

Total internal reflection microscopy: examination of competitive schemes via discrete sources method

Elena Eremina¹, Yuri Eremin², Natalia Grishina²
and Thomas Wriedt³

¹ Institute of Materials Science, University of Bremen, Badgasteiner straÙe 3, D-28359 Bremen, Germany

² Faculty of Computational Mathematics and Cybernetics, Moscow Lomonosov State University, Vorobyov's Hills, Moscow 119991, Russia

³ Institut für Werkstofftechnik, Badgasteiner straÙe 3, D-28359 Bremen, Germany

E-mail: eremina@iwt.uni-bremen.de

Received 22 March 2010, accepted for publication 16 July 2010

Published 23 August 2010

Online at stacks.iop.org/JOpt/12/095703

Abstract

The discrete sources method has been applied to perform a computer simulation analysis of different total internal reflection microscopy schemes. It has been found that the positioning of the objective lens beneath a glass prism can provide a considerable advantage for determination of the particle–film distance.

Keywords: total internal reflection microscopy, evanescent waves scattering, discrete sources method

(Some figures in this article are in colour only in the electronic version)

1. Introduction

Total internal reflection microscopy (TIRM) is a relatively new non-invasive technique to measure weak interaction forces between colloidal particles and a plane surface with a resolution down to a few femtonewtons [1, 2]. The high sensitivity of TIRM compared to other techniques like atomic force microscopy [3] is due to the use of the Brownian fluctuations of a free colloidal particle for obtaining the interaction potential. Compared to photonic force microscopy (PFM) [4, 5], which is able to measure femtonewton forces as well, TIRM is suitable for measurements close to surfaces, while the PFM is applicable just to the bulk measurements far from any surface. Recently TIRM has been applied to measure van der Waals [6], Casimir [7], magnetic [8], depletion [9, 10] and electrostatic [11] forces.

In the first years of TIRM measurements the reconstruction of the interaction potential was based on the assumption that the intensity of the field scattered by a particle near the surface was proportional to the intensity of an evanescent field in that area. However, later measurements found a discrepancy in the behaviour of observed interaction potentials for P and S polarized light [12]. It was found that this difference was

caused by particle–surface scattering interaction which has not been taken into account by the simple model. To account for this scattering interaction it has been suggested to use an exact scattering model, based on the discrete sources method (DSM) [13]. It has been shown that the use of such an exact model allows reconstruction of the potential with high precision [12, 14].

In a conventional TIRM set-up the colloidal particle is situated above the glass prism. The laser beam propagating in the prism with an angle slightly above the angle of total internal reflection to the surface produces an evanescent field in the area above the prism. The scattered light is collected by a detector positioned in the liquid medium above the particle. Recently there arose the idea to put the light collector in the area beneath the glass prism. In this set-up the collector's objective is looking towards the beam, reflected from the surface. To reduce the intensity of the reflected beam it was suggested to use the effect of surface plasmon resonance (SPR) in a thin gold film, deposited on the prism surface.

In the present work the DSM has been applied to model both schemes of TIRM set-up to choose the most effective one for particle–film distance determination. It has been found that the positioning of the collector beneath the prism provides an advantage compared with the conventional scheme.

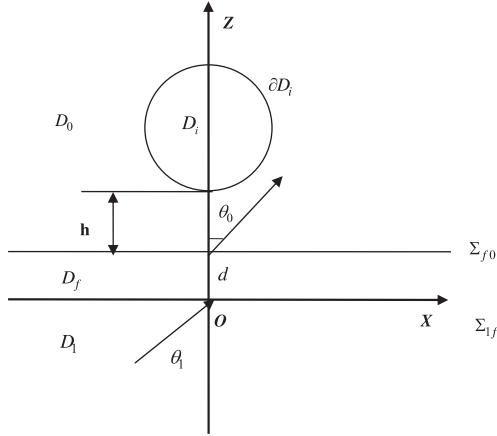


Figure 1. Model geometry: particle deposited on a filmed prism surface.

In the next part of the paper we will give a short introduction to the theory of the DSM and in the third part numerical results are presented and discussed.

2. Scattering problem statement

In this section we start with the mathematical statement of the scattering problem. Consider a glass prism occupying a half-space $D_1, z < 0$ with a metal film domain $D_f, d > z > 0$ of thickness d and a spherical penetrable particle with interior domain D_i and smooth boundary ∂D_i that is deposited above the film in the domain $D_0, z > d$ (figure 1).

Let us now introduce a Cartesian coordinate system $Oxyz$ by choosing its origin O at the prism surface Σ_{f0} such that the z axis coincides with the axis of symmetry of the particle and is directed into the domain D_0 . We assume that the exciting field $\{\mathbf{E}^0, \mathbf{H}^0\}$ is a linear polarized plane wave propagating inside the glass prism at angle θ_1 with respect to the z axis. Then the mathematical statement of the scattering problem can be formulated in the following form:

$$\begin{aligned} \nabla \times \mathbf{H}_\zeta &= jk\varepsilon_\zeta \mathbf{E}_\zeta; & \nabla \times \mathbf{E}_\zeta &= -jk\mu_\zeta \mathbf{H}_\zeta \\ & \text{in } D_\zeta, & \zeta &= 0, f, 1, i, \\ \mathbf{n}_i \times \begin{cases} (\mathbf{E}_i(p) - \mathbf{E}_0(p)) = 0 \\ (\mathbf{H}_i(p) - \mathbf{H}_0(p)) = 0 \end{cases} & p \in \partial D_i, & (1) \\ \mathbf{e}_z \times \begin{cases} (\mathbf{E}_\alpha(p) - \mathbf{E}_\beta(p)) = 0 \\ (\mathbf{H}_\alpha(p) - \mathbf{H}_\beta(p)) = 0 \end{cases} & p \in \sum_{\alpha\beta} \end{aligned}$$

and radiation conditions at infinity for scattered field in D_0, D_1 and attenuation conditions in D_f .

Here, \mathbf{n}_i is the outward unit normal vector to the surface ∂D_i , $k = \omega/c$ and $\{\mathbf{E}_\zeta, \mathbf{H}_\zeta\}$ stands for the total field in the corresponding domain D_ζ , \mathbf{e}_z is the unit vector along the z axis, $\sum_{\alpha\beta}$ is the plane interface between domains D_α and D_β , $\alpha, \beta = 0, 1, f$, ε_ζ is the media permittivity and μ_ζ is the permeability. Note that the total field in D_0 is a superposition of the refracted exciting plane wave and the scattered field. If $\text{Im} \varepsilon_\zeta, \mu_\zeta \leq 0$ (time dependence for the fields is chosen as $\exp[j\omega t]$) and the particle surface is smooth enough, $\partial D_i \subset C^{(2,\alpha)}$, then the boundary-value problem (1) is uniquely solvable.

The solution of the boundary-value problem is constructed following the DSM scheme [13]. The advantage of the DSM is that it is a semi-analytical meshless method and it does not require any integration procedure. First the diffraction problem of the plane wave $\{\mathbf{E}^0, \mathbf{H}^0\}$ on the layered interface is solved. The resulting field $\{\mathbf{E}_\zeta^0, \mathbf{H}_\zeta^0\}$ satisfies the transmission conditions at Σ_{1f} and Σ_{f0} . Then we construct an approximate solution of the problem (1) for the scattered field $\{\mathbf{E}_\zeta^s, \mathbf{H}_\zeta^s\}$ in domains $D_\zeta, \zeta = 0, f, 1$ and the total field inside the particle D_i . Following the DSM scheme the electromagnetic fields are represented as a finite linear combination of fields of multipoles which analytically satisfy the transmission conditions enforced at the plane interfaces Σ_{1f} and Σ_{f0} [15]. So, the approximate solution satisfies the Maxwell equations in domains $D_{0,1,f,i}$, the infinity conditions and the transmission conditions at the plane interfaces. Thus, the scattering problem is reduced to the problem of approximating the exciting field on the particle's surface ∂D_i . The amplitudes of discrete sources (DS) are determined from the boundary conditions at the particle surface, which can be rewritten as

$$\begin{aligned} \mathbf{n}_p \times (\mathbf{E}_i - \mathbf{E}_0^s) &= \mathbf{n}_p \times \mathbf{E}_0^0, \\ \mathbf{n}_p \times (\mathbf{H}_i - \mathbf{H}_0^s) &= \mathbf{n}_p \times \mathbf{H}_0^0 \quad \text{at } \partial D_i. \end{aligned} \quad (2)$$

To construct the fields of dipoles and multipoles that analytically satisfy the transmission conditions at the plane interfaces Σ_{1f} and Σ_{f0} the Green's tensor for a stratified interface is applied (see the appendix).

Once the DS amplitudes are determined, one can compute the far-field pattern $\mathbf{F}_{0,1}(\theta, \varphi)$ in $D_{0,1}$ domains:

$$\begin{aligned} \mathbf{F}_{0,1}^s(M)/|\mathbf{E}^0(z=0)| &= \frac{\exp\{-jk_{0,1}r\}}{r} \mathbf{F}_{0,1}(\theta, \varphi) + o(r^{-1}), \\ r = |M| &\rightarrow \infty \end{aligned}$$

where $\mathbf{F}_{0,1}(\theta, \varphi)$ are determined at a unit sphere and have two components corresponding to P/S polarized excitation: $\mathbf{F}_{0,1}^{P,S}(\theta, \varphi) = F_{0,1(\theta)}^{P,S} \mathbf{e}_\theta + F_{0,1(\varphi)}^{P,S} \mathbf{e}_\varphi$.

By asymptotical evaluation of the Weyl-Sommerfeld integrals involved in the scattered field representation the far-field pattern components for P-polarization accept the following form [13]:

$$\begin{aligned} F_{0,1(\theta)}^P(\theta, \varphi) &= jk \sum_{m=0}^M (jk_{0,1} \sin \theta)^m \cos(m+1)\varphi \\ &\times \sum_{n=1}^{N_m} \left\{ p_{nm}^P [\bar{G}_n^{e(0,1)} \cos \theta + jk_{0,1} \sin^2 \theta \bar{g}_n^{e(0,1)}] \right. \\ &\left. + \sqrt{\frac{\mu_{0,1}}{\varepsilon_{0,1}}} q_{nm}^P \bar{G}_n^{h(0,1)} \right\} - jk \sin \theta \sum_{n=1}^{N_0} r_n^P \bar{G}_n^{h(0,1)}, \\ F_{0,1(\varphi)}^P(\theta, \varphi) &= -jk \sum_{m=0}^M (jk_{0,1} \sin \theta)^m \sin(m+1)\varphi \\ &\times \sum_{n=1}^{N_m} \left\{ p_{nm}^P \bar{G}_n^{e(0,1)} + \sqrt{\frac{\mu_{0,1}}{\varepsilon_{0,1}}} q_{nm}^P [\bar{G}_n^{h(0,1)} \cos \theta \right. \\ &\left. + jk_{0,1} \sin^2 \theta \bar{g}_n^{h(0,1)}] \right\}, \end{aligned}$$

for S-polarized excitation:

$$F_{0,1(\theta)}^S(\theta, \varphi) = jk \sum_{m=0}^M (jk_{0,1} \sin \theta)^m \sin(m+1)\varphi$$

$$\times \sum_{n=1}^N \left\{ p_{nm}^S [\bar{G}_n^{e(0,1)} \cos \theta + jk_{0,1} \sin^2 \theta \bar{g}_n^{e(0,1)}] - \sqrt{\frac{\mu_{0,1}}{\varepsilon_{0,1}}} q_{nm}^S \bar{G}_n^{h(0,1)} \right\}$$

$$F_{0,1(\varphi)}^S(\theta, \varphi) = jk \sum_{m=0}^M (jk_{0,1} \sin \theta)^m \cos(m+1)\varphi$$

$$\times \sum_{n=1}^N \left\{ p_{nm}^S \bar{G}_n^{e(0,1)} - \sqrt{\frac{\mu_{0,1}}{\varepsilon_{0,1}}} q_{nm}^S [\bar{G}_n^{h(0,1)} \cos \theta + jk_{0,1} \sin^2 \theta \bar{g}_n^{h(0,1)}] \right\} + jk \sqrt{\frac{\mu_{0,1}}{\varepsilon_{0,1}}} \sin \theta \sum_{n=1}^N r_n^S \bar{G}_n^{e(0,1)},$$

where $\{p_{nm}^{P,S}, q_{nm}^{P,S}, r_n^{P,S}\}$ are the Fourier harmonics of the DS amplitudes corresponding to P/S polarizations and $\bar{G}_n^{e,h(0,1)}, \bar{g}_n^{e,h(0,1)}$ are spectral functions accepting the form

$$\bar{G}_n^{e,h(0)} = \exp\{jk_0 z_n \cos \theta\} + jk_0 \cos \theta \exp\{jk_0 d \cos \theta\}$$

$$\times A_{11}^{e,h}(k_0 \sin \theta, z_n),$$

$$\bar{G}_n^{e,h(1)} = jk_1 \cos \theta D_{11}^{e,h}(k_1 \sin \theta, z_n),$$

$$\bar{g}_n^{e,h(0)} = jk_0 \cos \theta \exp\{jk_0 d \cos \theta\} A_{31}^{e,h}(k_0 \sin \theta, z_n),$$

$$\bar{g}_n^{e,h(1)} = jk_1 \cos \theta D_{31}^{e,h}(k_1 \sin \theta, z_n).$$

Hence, after the unknown amplitudes of DS are determined, the far-field patterns for P and S polarization are represented as finite linear combinations of elementary functions. This circumstance ensures fast and effective computer analysis of scattering characteristics in the far zone.

3. Results and discussion

In this section we present some computer simulation results for the conversion of evanescent waves into scattered ones by a particle deposited above a metal-filmed glass prism. We consider the differential scattering cross section (DSC), which is given by

$$DSC_{0,1}^{P,S}(\theta_1, \theta, \varphi) = |F_{0,1(\theta)}^{P,S}(\theta_1, \theta, \varphi)|^2 + |F_{0,1(\varphi)}^{P,S}(\theta_1, \theta, \varphi)|^2. \quad (3)$$

The dimension of $DSC_{0,1}^{P,S}$ is in μm^2 units. In this paper we also examine the objective response as a function of the height of the particle. It represents the integrated intensity scattered into the prescribed solid angle Ω :

$$\sigma_{0,1}^{P,S}(\theta_1) = \int_{\Omega} DSC_{0,1}^{P,S}(\theta_1, \theta, \varphi) d\omega, \quad (4)$$

where Ω corresponds to the numerical aperture of an objective lens. The integral response is used to evaluate the scattered intensity captured by the objective lens [10].

In this work we will consider P or S polarized plane waves with a wavelength of $\lambda = 633$ nm. The prism is made of LASF46A glass with a refractive index for this wavelength of $n_1 = 1.904$. The particles we consider are made of polystyrene

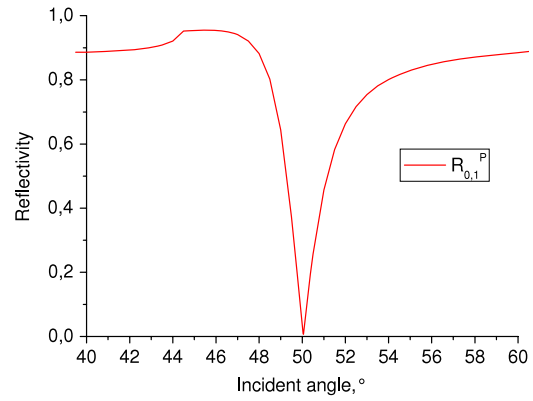


Figure 2. Reflection coefficient R_{01}^P (5) from prism–film interface for P polarized plane wave in water.

latex $n_i = 1.59$ and have diameters of $D = 300$ nm, 600 nm and 1.2 μm . Particles are situated in water with $n_0 = 1.33$ on a gold film with $n_f = 0.18-3.26j$ and a thickness of $d = 49$ nm. The gold film enables us to increase the penetration depth (up to 720 nm) and light reflectivity [16]. The critical angle for this system at which evanescent waves appear is 44.31° . Scattered fields are captured by the objectives with collecting angles of 23° and 32° . For technical reasons, the collector situated beneath the prism has a central cut of 5° to avoid the specular beam.

Corresponding to Snell’s law: $n_0 \sin \theta_0 = n_1 \sin \theta_1$. When the incident angle exceeds the critical one $\theta_1 > \theta_c = \arcsin(n_1/n_0)$, $n_1 > n_0$ the exciting wave is totally reflected from the upper interface Σ_{f0} and only an evanescent wave propagating along the plane surface Σ_{f0} and damped along the z direction is present in D_0 . Here we would like to emphasize that the critical angle of the system does not depend on an additional gold film.

As is known the SPR corresponds to a minimum value of the reflection coefficient from the prism–film interface for a P polarized plane wave in water R_{01}^P (figure 2). This appears behind the angle of total internal reflection $\theta_1 > \theta_c$:

$$R_{01}^P(\theta_1) = \frac{r_{1f}^P + r_{f0}^P \exp\{-2jk_f \cos \theta_f d\}}{1 + r_{1f}^P r_{f0}^P \exp\{-2jk_f \cos \theta_f d\}}. \quad (5)$$

Here r_{1f}, r_{f0} are reflection coefficients from boundaries Σ_{1f}, Σ_{f0} and θ_f is the angle of refraction into the film.

In the following figures the results of computer simulation analysis are presented. In figure 3 the objective response $\sigma_{0,1}^{P,S}$ versus particle–film distance h is presented for several particles and both polarizations of the incident light. The capturing objective with a collecting angle of 32° is situated beneath the prism. We can see that all the curves demonstrate monotonic exponential decay. To compare to these results we present similar computations for the case when the collector is situated above the prism (figure 4).

Now we observe completely different behaviour: all the curves demonstrate pronounced oscillations. For some of them (e.g. for particles of $D = 300$ nm) the fluctuation of values is so extreme that at three different heights the value of σ_0^P is nearly the same. This last fact makes the problem of an exact

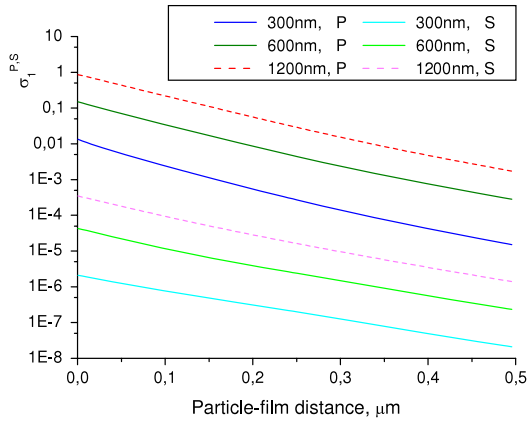


Figure 3. Integrated intensity (4) for particles of different diameters for collector beneath the prism, and P and S polarizations of the incident light.

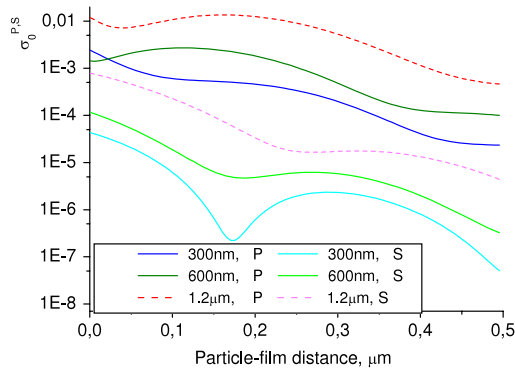


Figure 4. Integrated intensity for particles of different diameters for collector above the prism, and P and S polarizations.

particle height determination from the measured data above the film impossible without additional information. Similar oscillations have been detected in [17].

In figure 5 the results are presented for the particle of $D = 300$ nm for both positions of the collector with capturing angle 32° . The results demonstrate that the intensity of P-polarized light is several orders higher than for the S-polarized one. Similarly to the results presented above, both curves for the upper collector show oscillations, while both curves for the collector beneath the prism have monotonic exponential decay. Similar results but for larger particles of $D = 600$ nm (figure 6) and $D = 1.2 \mu\text{m}$ (figure 7) are presented as well.

To investigate what kind of influence the numerical aperture of the collector has, in figures 8 and 9 the numerical results for the particle of $D = 1.2 \mu\text{m}$ are presented for two collecting angles, 23° and 32° , of the collectors deposited beneath (figure 8) and above (figure 9) the prism. The results demonstrate that the scattering behaviour of the curves stays the same and just the intensity depends on the objective's aperture. In the following results we will use only objectives with collecting angles of 32° .

Now we would like to analyse the behaviour of the DSC in the incidence plane. For these investigations we took two

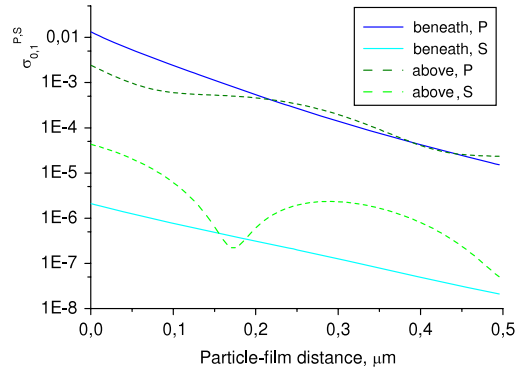


Figure 5. Integrated intensity for particle $D = 300$ nm collectors beneath and above the prism, and P and S polarizations.

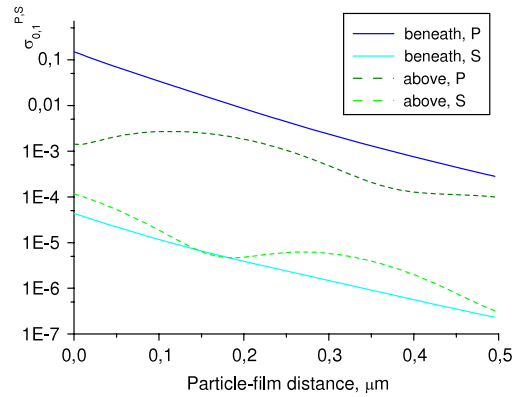


Figure 6. Integrated intensity for particle $D = 600$ nm collectors beneath and above the prism, and P and S polarizations.

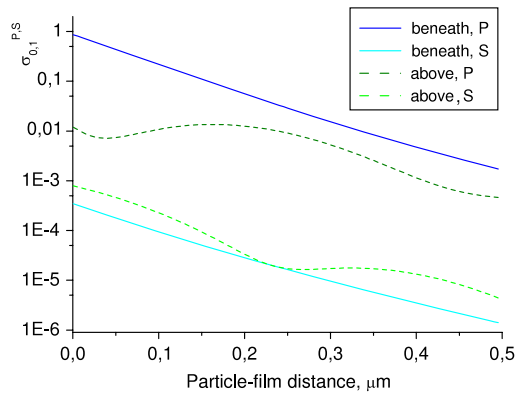


Figure 7. Integrated intensity for particle $D = 1.2 \mu\text{m}$ collectors beneath and above the prism, and P and S polarizations.

particle heights where σ_0^P has close values. The results for DSC distribution for the particle of $D = 600$ nm are presented in figure 10. Here the range of observation angles $90^\circ < \theta < 270^\circ$ belongs to the upper semi-plane (water) and the range of $270^\circ < \theta < 360^\circ$ belongs to the lower semi-plane.

From the figure it is obvious that the maximum of intensity is directed towards the specular direction at $\theta \approx 130^\circ$. From the comparison it is also easy to see that the difference of the intensity scattered to the upper semi-plane is much lower

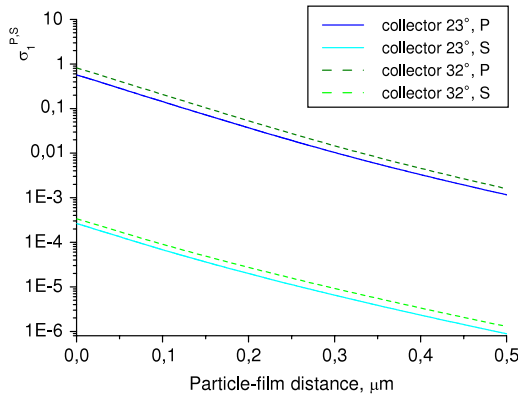


Figure 8. Integrated intensity for particle $D = 1.2 \mu\text{m}$ for collectors with different collecting angles beneath the prism, and P and S polarizations.

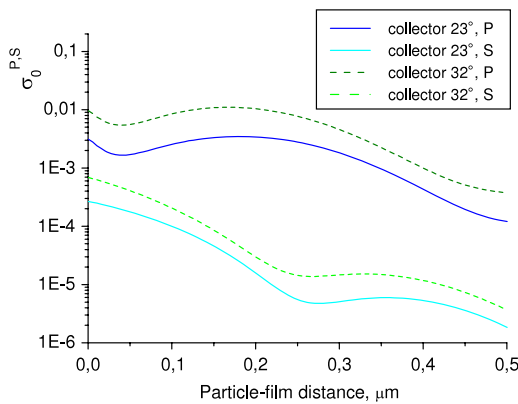


Figure 9. Integrated intensity for particle $D = 1.2 \mu\text{m}$ for collectors with different collecting angle above the prism, and P and S polarizations.

than the intensity at $\theta \approx 130^\circ$, regardless that the central 5° of the objective lens is blocked to omit the specular beam. Similar results are presented for the particle of $D = 300 \text{ nm}$ (figure 11). Here it was possible to choose the heights so that not only the values of DSC for both heights of the upper collector were close, but for the height $h = 215 \text{ nm}$ the values of both DCS curves for the collector situated above and beneath the prism were the same. From the results presented above we see that, in spite of the upper semi-plane, the intensity values are nearly the same, while at the lower semi-plane both values differ essentially. Due to this fact the determination of the particle–film distance from observations of the intensity beneath the prism should be much easier, in contrast to the conventional observations in the upper domain.

4. Conclusion

In this paper two different schemes for a TIRM set-up are modelled and discussed. The TIRM scheme with the collector deposited beneath the prism gives considerable advantages. From the presented modelling results it is clear that the scattered intensity beneath the prism is higher than above the particle. Additionally the behaviour of the DCS

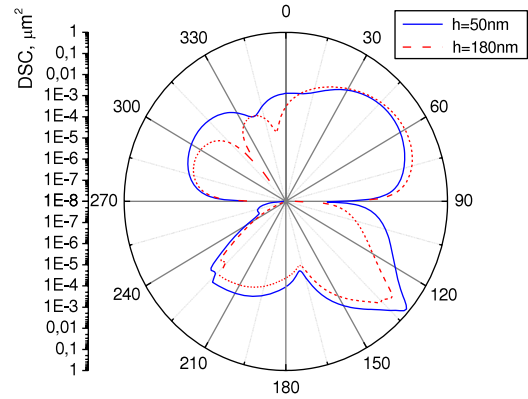


Figure 10. Scattered intensity in the incidence plane for the particle of $D = 600 \text{ nm}$ for different particle–film distances h , P polarization.

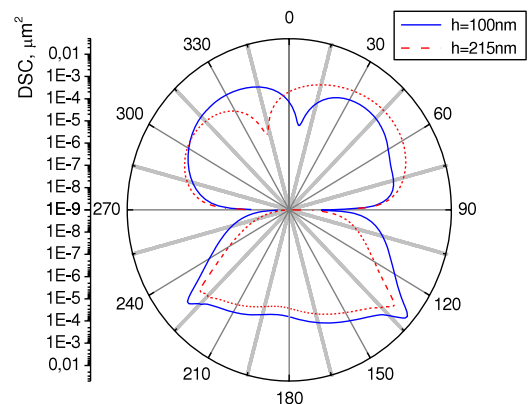


Figure 11. Scattered intensity in the incidence plane for the particle of $D = 300 \text{ nm}$ for different h , P polarization.

curves observed beneath the prism demonstrates monotonic exponential decay that enables easier determination of the particle–film distance. It seems that the alternative TIRM scheme is more advantageous than the conventional one and should be taken into account when setting up new TIRM measurements.

Acknowledgments

We gratefully acknowledge funding of this research by Deutsche Forschungsgemeinschaft (DFG) and the Russian Foundation for Basic Research (RFBR).

Appendix. Discrete sources method

The discrete sources method is an effective tool for analysis of light scattering by local features deposited near a stratified interface [13]. The field of the discrete sources is constructed based on the Green’s tensor for a stratified interface [15]:

$$\overset{\leftrightarrow}{\mathbf{G}}^{e,h}(M, M_0) = \begin{bmatrix} G^{e,h} & 0 & 0 \\ 0 & G^{e,h} & 0 \\ \partial g^{e,h}/\partial x_M & \partial g^{e,h}/\partial y_M & G^{h,e} \end{bmatrix}.$$

The Green's tensor components can be represented in the form of Sommerfeld integrals:

$$G^{e,h}(M, M_0) = \int_0^\infty J_0(\lambda r) v_{11}^{e,h}(\lambda, z, z_0) \lambda d\lambda,$$

$$g^{e,h}(M, M_0) = \int_0^\infty J_0(\lambda r) v_{31}^{e,h}(\lambda, z, z_0) \lambda d\lambda$$

where $r^2 = \rho^2 + \rho_0^2 - 2\rho\rho_0 \cos(\varphi - \varphi_0)$, $J_0(\cdot)$ is a Bessel function and (ρ_0, φ_0, z_0) are cylindrical coordinates of M_0 . Corresponding spectral functions $v_{11}^{e,h}, v_{31}^{e,h}$ providing transmission conditions enforced at $z = 0, d$ have the following forms:

$$v_{11}^{e,h}(\lambda, z, z_0) = \begin{cases} \frac{\exp\{-\eta_0|z - z_0|\}}{\eta_0} + A_{11}^{e,h}(\lambda, z_0) \\ \quad \times \exp\{-\eta_0|z - d|\}, & z \geq d, \quad z_0 > 0, \\ B_{11}^{e,h}(\lambda, z_0) \exp\{-\eta_f|z - d|\} \\ \quad + C_{11}^{e,h}(\lambda, z_0) \exp\{-\eta_f z\}, & d \geq z \geq 0 \\ D_{11}^{e,h}(\lambda, z_0) \exp\{\eta_f z\}, & z \leq 0, \end{cases}$$

$$v_{31}^{e,h}(\lambda, z, z_0) = \begin{cases} A_{31}^{e,h}(\lambda, z_0) \exp\{-\eta_0|z - d|\}, & z \geq d, \quad z_0 > 0, \\ B_{31}^{e,h}(\lambda, z_0) \exp\{-\eta_f|z - d|\} \\ \quad + C_{31}^{e,h}(\lambda, z_0) \exp\{-\eta_f z\}, & d \geq z \geq 0 \\ D_{31}^{e,h}(\lambda, z_0) \exp\{\eta_f z\}, & z \leq 0, \end{cases}$$

where $\eta_\zeta^2 = \lambda^2 - k_\zeta^2, k_\zeta = k\sqrt{\varepsilon_\zeta \mu_\zeta}$. The associated coefficients A, B, C and D are determined from the following conditions at $z = 0, d$:

$$[v_{11}^e] = \left[\frac{1}{\mu} \frac{\partial v_{11}^e}{\partial z} \right] = 0;$$

$$[v_{11}^h] = \left[\frac{1}{\varepsilon} \frac{\partial v_{11}^h}{\partial z} \right] = 0;$$

$$\left[\frac{1}{\mu} v_{31}^e \right] = 0; \quad \left[\frac{1}{\varepsilon \mu} \frac{\partial v_{31}^e}{\partial z} \right] = - \left[\frac{1}{\varepsilon \mu} \right] v_{11}^e;$$

$$\left[\frac{1}{\varepsilon} v_{31}^h \right] = 0; \quad \left[\frac{1}{\varepsilon \mu} \frac{\partial v_{31}^h}{\partial z} \right] = - \left[\frac{1}{\varepsilon \mu} \right] v_{11}^h.$$

More details can be found in [13]. Let us consider a P-polarized exciting plane wave. In this case, the refracted plane wave in D_0 accepts the following form:

$$\mathbf{E}_0^0 = T_{01}^P(-\mathbf{e}_x \cos \theta_0 + \mathbf{e}_z \sin \theta_0) \\ \times \exp\{-jk_0(x \sin \theta_0 + z \cos \theta_0)\},$$

$$\mathbf{H}_0^0 = -T_{01}^P n_0 \mathbf{e}_y \exp\{-jk_0(x \sin \theta_0 + z \cos \theta_0)\},$$

where $(\mathbf{e}_x, \mathbf{e}_y, \mathbf{e}_z)$ are unit vectors of the Cartesian coordinate system and T_{01}^P is the transmission coefficient for P polarization corresponding to the multi-layered interface:

$$T_{01}^P = \frac{t_{1f}^P t_{f0}^P \exp(-jk_f \cos \theta_f d)}{1 + r_{1f}^P r_{f0}^P \exp(-2jk_f \cos \theta_f d)}.$$

Here $n_\zeta = \sqrt{\varepsilon_\zeta \mu_\zeta}$ is the refractive index; θ_ζ is an angle of refraction inside $D_\zeta, \zeta = 0, f$ and

$$t_{\alpha\beta}^P = \frac{2n_\alpha \cos \theta_\alpha}{n_\alpha \cos \theta_\beta + n_\beta \cos \theta_\alpha},$$

$$r_{\alpha\beta}^P = \frac{n_\alpha \cos \theta_\beta - n_\beta \cos \theta_\alpha}{n_\alpha \cos \theta_\beta + n_\beta \cos \theta_\alpha}.$$

Consider now S-polarized excitation. Then the refracted plane wave in D_0 accepts the form

$$\mathbf{E}_0^0 = T_{01}^S \mathbf{e}_y \exp\{-jk_0(x \sin \theta_0 + z \cos \theta_0)\},$$

$$\mathbf{H}_0^0 = T_{01}^S n_0 (-\mathbf{e}_x \cos \theta_0 + \mathbf{e}_z \sin \theta_0) \\ \times \exp\{-jk_0(x \sin \theta_0 + z \cos \theta_0)\},$$

where

$$T_{01}^S = \frac{t_{1f}^S t_{f0}^S \exp(-jk_f \cos \theta_f d)}{1 + r_{1f}^S r_{f0}^S \exp(-2jk_f \cos \theta_f d)}$$

and

$$t_{\alpha\beta}^S = \frac{2n_\alpha \cos \theta_\alpha}{n_\alpha \cos \theta_\alpha + n_\beta \cos \theta_\beta},$$

$$r_{\alpha\beta}^S = \frac{n_\alpha \cos \theta_\alpha - n_\beta \cos \theta_\beta}{n_\alpha \cos \theta_\alpha + n_\beta \cos \theta_\beta}.$$

An approximate solution of the scattering problem based on the DSM is constructed fulfilling the transmission conditions on plane interfaces Σ_{1f} and Σ_{f0} , and taking into account both the rotational symmetry of the scattering problem geometry (particle plus layered interface) and the polarization of the exciting field [13]. It is represented as a finite linear combination of the lowest order multipoles distributed over the axis of symmetry or deposited in a complex plane [18]. In this case it accepts the form of a finite Fourier series with respect to the azimuth variable φ . Resolving the fields of refracted plane waves in Fourier series

$$\exp\{-jk_0 \rho \sin \theta_0 \cos \varphi\} \\ = \sum_{m=0}^{\infty} (2 - \delta_{0m}) (-j)^m J_m(k_0 \rho \sin \theta_0) \cos m\varphi$$

where δ_{0m} is the Kronecker symbol and J_m is the Bessel function of order m , we proceed from the surface approximation problem (2) to a set of one-dimensional approximating problems enforced at the particle meridian [13]. Besides, the DSM enables us to employ different numbers of basic functions for the representation of the scattered and the internal fields, which provides a possibility to examine scattering obstacles with high refractive indices. To fit the transmission conditions at the particle meridian the generalized point-matching technique is employed with a distribution of matching points over the surface meridian. This provides a reduction of the sizes of linear systems under consideration and leads to a reduction of the computational time and memory storage. The amplitudes of multipoles are determined as pseudo-solutions of over-determined systems of linear equations. To provide the full rank of a rectangular matrix of the over-determined system a regularization procedure is applied. We use a complex shift of the spectrum of the extended rectangular matrix, which enables us to get a normal pseudo-solution. The completeness of the system of

lowest order distributed multipoles guarantees convergence of the approximate solution to the exact one in any closed subset of $D_{0,1}$. The additional advantage of the DSM-based numerical scheme consists in the possibility to estimate errors of the approximate solution. For this the surface residual is evaluated, thus tracking the convergence of the real results [13].

References

- [1] Walz J 1997 Measuring particle interactions with total internal reflection microscopy *Curr. Opin. Colloid Interface Sci.* **2** 600–6
- [2] Prieve D C 1999 Measurement of colloidal forces with TIRM *Adv. Colloid Interface Sci.* **82** 93–125
- [3] Ducker W, Senden T and Pashley R 1991 Direct measurement of colloidal forces using an atomic force microscope *Nature* **353** 239–41
- [4] Berg-Sørensen K and Flyvbjerg H 2004 Power spectrum analysis for optical tweezers *Rev. Sci. Instrum.* **75** 594–612
- [5] Volpe G, Volpe G and Petrov D 2007 Brownian motion in a nonhomogeneous force field and photonic force microscope *Phys. Rev. E* **76** 118
- [6] Bevan M A and Prieve D C 1999 Direct measurement of retarded van der Waals attraction *Langmuir* **15** 7925–36
- [7] Hertlein C, Helden L, Gambassi A, Dietrich S and Bechinger C 2008 Direct measurement of critical Casimir forces *Nature* **451** 172–5
- [8] Blickle V, Babić D and Bechinger C 2005 Evanescent light scattering with magnetic colloids *Appl. Phys. Lett.* **87** 101–2
- [9] Piech M, Weroniński P, Wu X and Walz J Y 2002 Prediction and measurement of the interparticle depletion interaction next to a flat wall *J. Colloid Interface Sci.* **247** 327–41
- [10] Helden L, Roth R, Koenderink G H, Leiderer P and Bechinger C 2003 Direct measurement of entropic forces induced by rigid rods *Phys. Rev. Lett.* **90** 301
- [11] Von Grünberg H H, Helden L, Leiderer P and Bechinger C 2001 Measurement of surface charge densities on Brownian particles using total internal reflection microscopy *J. Chem. Phys.* **114** 10094–104
- [12] Helden L, Eremina E, Eremin Y, Riefler N, Hertlein C, Bechinger C and Wriedt T 2006 Single particle evanescent light scattering simulations for total internal reflection microscopy *Appl. Opt.* **45** 7299–308
- [13] Eremin Y 2000 The method of discrete sources in electromagnetic scattering by axially symmetric structures *J. Commun. Technol. Electron.* **45** (Supp 2) S269–80
- [14] Hertlein C, Riefler N, Eremina E, Wriedt T, Eremin Y, Helden L and Bechinger C 2008 Experimental verification of an exact evanescent light scattering model for TIRM *Langmuir* **24** 1–4
- [15] Eremin Y and Wriedt T 2004 Discrete sources method model for evanescent waves scattering analysis *J. Quant. Spectrosc. Radiat. Transfer* **89** 53–65
- [16] Volpe G, Brettschneider T, Helden L and Bechinger C 2009 Novel perspectives for the application of total internal reflection microscopy *Opt. Express* **17** 23975
- [17] Eremina E, Grishina N, Eremin Y, Helden L and Wriedt T 2006 Total internal reflection microscopy with multilayered interface: light scattering model based on discrete sources method *J. Opt. A: Pure Appl. Opt.* **8** 999–1006
- [18] Doicu A, Eremin Yu and Wriedt T 2000 *Acoustic and Electromagnetic Scattering Analysis Using Discrete Sources* (London: Academic)